Effective Utilization of Nanoporosity and Surface Area Guides Electrosynthesis over Soft-Landed Copper Oxide Catalyst Layers

Sven Arnouts[ab†], Daniel Choukroun[a†], Ilargi Napal[c,d], Guillermo Tajuelo Castilla[e], Javier Prieto[e], Nathalie Claes[b], Nick Daems[a], Silvia Nappini[c], Elena Magnano[c,f], Gonzalo Santoro[g], Sara Bals[b], José Ángel Martín-Gago[e], Tom Breugelmans[a*]

[a] *Applied Electrochemistry and Catalysis (ELCAT), University of Antwerp, 2610 Wilrijk, Belgium.*

[b] *Electron Microscopy for Materials Science (EMAT) and Nanolight, University of Antwerp, 2020 Antwerp, Belgium.*

[c] *IOM CNR Laboratorio TASC, 34149 Basovizza. Trieste, Italy.*

[d] *Università degli Studi di Trieste, Physics Department, 34127 Trieste, Italy*

[e] *Instituto de Ciencia de Materiales de Madrid (ICMM), CSIC, 28049 Madrid, Spain.*

[f] *Nanotechnology Research Laboratory, Faculty of Engineering, University of Sydney, Camperdown 2006, Australia*

[g] *Instituto de Estructura de la Materia (IEM), CSIC, 28006 Madrid, Spain*

† These authors contributed equally to this work.

* Corresponding author

E-mail address: Tom.Breugelmans@uantwerpen.be

ABSTRACT

Porous nanomaterials find wide-ranging applications in modern medicine, optoelectronics and catalysis, playing a key role in today's effort to build an electrified, sustainable future. Accurate in-situ quantification of their structural and surface properties is required to model their performance and improve their design. In this article, we demonstrate how to assess the porosity, surface area and utilization of a model nanoporous soft-landed copper oxide catalyst layer/carbon interface, which is otherwise difficult to resolve using physisorption or capacitance-based methods. Our work employs electron tomography to characterize the three-dimensional structure of the catalyst layer and combines it with in-situ soft X-ray absorption spectroscopy and lead underpotential deposition data to probe the stability and utilization of the catalyst layer under potential bias. The analysis proves that a significant share of the original surface area is exploited, and thus explains product distribution and crossover trends in the electrosynthesis of C_2 products from carbon monoxide.

KEYWORDS

Nanoporous catalyst layers, electrosynthesis, electron tomography, in-situ analysis, CO reduction

MAIN

Porous nanomaterials find wide-ranging applications in modern optoelectronics, medicine and catalysis. As (electro)catalytic reagents, they play a key role in today's effort to intensify and electrify traditional chemical processes. In particular, copper-based catalysts show unique activity and selectivity in a variety of electro-synthetic reduction reactions that could sustainably yield chemicals such as urea, ethylene, ethanol, ammonia and 2,5-bishydroxymethylfuran.[1,2] Clearly, accurate quantification of structural properties such as porosity and specific surface area is required for calculating effective transport properties such as diffusivity, tortuosity and permeability and to establish structure-performance relationships.[3–5] Nowadays, established and emerging electrochemical energy conversion technologies such as polymer electrolyte fuel cells and low-temperature carbon dioxide and carbon monoxide reduction (COR) turn to nanostructured thin-film catalyst layers (CLs) to unlock high mass activity, short diffusion paths and more optimal water management.[6–9] Analysis of such nanoscopic interfaces by conventional methods such as nitrogen physisorption and double layer capacitance measurements is often compounded by the nanometric dimensions of those layers, the associated low material loading and the presence of a high surface area gas diffusion layer (GDL) background.

Over the past several years, novel approaches[10] based on microcomputed tomography (μCT)[11,12] and quartz crystal microbalances[13,14] have been developed to alleviate those issues and link the structural properties of CLs with performance.[15] Yet, difficulties in fabricating self-supporting nanoporous copper oxide CLs on GDLs have restricted that type of analysis to formulations containing ionomers[15] or hydrophobic polymers,[16] while the use of focused-ion-beam scanning electron microscopy (FIB-SEM) limited the attainable resolution.[17] In this article, we have addressed both challenges by employing electron tomography and an *in-situ* spectro-electrochemical analysis to yield a comprehensive characterization of nanoporous copper oxide CLs which were fabricated in a Sputtering Gas Aggregation Source (SGAS) and assembled bottom-up by soft-landing[18] Cu_2O and CuO nanocrystals (NCs) with controllable particle size and oxidation state onto gas diffusion layers. Additionally, we have linked the measured catalyst layer thickness, porosity and effective specific surface area with key COR performance indicators and compared them to those of nonporous continuous copper film analogues, which were fabricated using conventional magnetron sputtering. Our work ultimately quantifies how much of the originally prepared surface area is effectively utilized and how roughness impacts selectivity and product crossover under specific COR operating

conditions. In what follows, all catalyst layers will be named based on their type - either nanoporous (Cu_xO-NP) or continuous film (Cu-CF) - and Cu loading determined by inductively coupled plasma-mass spectrometry (ICP-MS), e.g. Cu_xO-NP-282 for a nanoporous Cu_xO layer with a loading of 282 $\mu g_{Cu} \cdot cm^{-2}$.

Cu_xO (x = 1-2) NCs were generated by means of SGAS using a Multiple Ion Cluster Source (MICS3, Oxford Applied Research Ltd., UK),[19–21] of which only a single magnetron and a 2" Cu target (99.99% purity) were employed.[22] To control the stoichiometry of Cu_xO NCs, O_2 was injected into the aggregation zone through a lateral entrance. Throughout this work, the source conditions which are annotated in Figure 1a (power, Ar flow rate, O_2 flow rate, aggregation distance) were kept fixed while the deposition time was varied in the range of 2 to 1800 s.

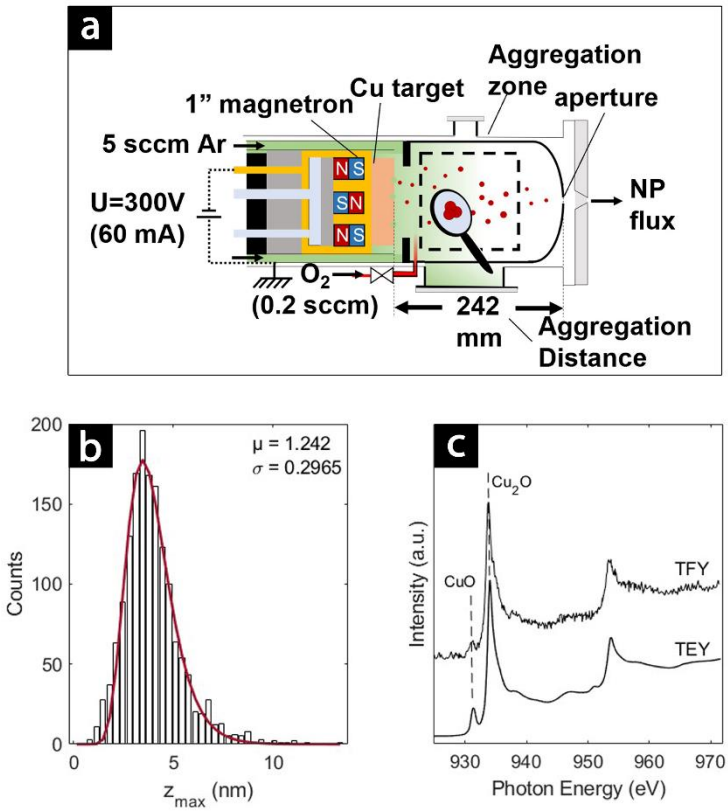

Figure 1 *(a) schematic representation of the MICS and experimental conditions: A total Ar flow rate of 100 sccm was used (5 sccm through the active magnetron and 95 sccm through the adjacent one). Magnetron power was 18 W and an O_2 flow rate of 0.2 sccm was injected into the aggregation zone with an aggregation distance (distance from the Cu target to the exit nozzle) of 242 mm; (b) lognormal particle size distribution of Cu_xO NCs on Si(100), deposition time: 2s, estimated loading: 0.5 $\mu g \cdot cm^{-2}$; (c) Cu $L_{3,2}$ absorption edge of Cu_xO NPs deposited onto Si_3N_4/Ti/Au membranes, deposition time: 60s, estimated loading: 7.5 $\mu g \cdot cm^{-2}$; in total electron yield (TEY) and total fluorescence yield (TFY) detection modes.*

We first investigated the morphological and electronic properties of dispersed Cu_xO NCs (0.5-2.5 $\mu g_{Cu} \cdot cm^{-2}$) and their assemblies (7.5 $\mu g_{Cu} \cdot cm^{-2}$) on flat substrates. Based on atomic force microscopy data (Figure S1), the NCs' diameter was found to be lognormally distributed[23]

with an expected value of 3.6 ± 0.3 nm, as shown in Figure 1b. In-situ X-ray photoelectron spectroscopy analysis (Figure S2) demonstrated that Cu_2O NCs were produced. This was further confirmed by *ex-situ* soft X-ray absorption spectroscopy (XAS) measurements at the Cu $L_{3,2}$ edge region, the results of which are depicted in Figure 1c. The pronounced absorption edge at 933.8 eV, which is detected in both surface- (total electron yield, TEY) and bulk-sensitive (total fluorescence yield, TFY) detection modes, is characteristic of the occupied $2p \rightarrow$unoccupied $3d^{10}/4s^0$ electronic transition of Cu_2O.[24] A minor contribution from CuO is attributed to the peak at 931.3 eV, a $2p \rightarrow 3d^9$ transition. Based on the absorption cross section of each peak and their measured intensities, the share of Cu_2O in the sample amounts to 96% (see Supporting Note 1, Table S1 and Figure S3).

We then studied the electronic (Supporting Note 2, Figure S4-S6) and morphological properties of nanoporous CLs that were assembled bottom-up by soft-landing Cu_xO nanocrystals onto carbon fiber and microporous gas diffusion layers (GDLs), which are the substrates for electrochemical COR. Figure 2a-c shows cross-sectional scanning electron microscopy (SEM) and transmission electron microscopy (TEM) images for Cu_xO-NP, exposing porous domains and morphological uniformity across the entire film. It is observed that the thickness of Cu_xO-NP CLs increases linearly with deposition time and thus Cu loading (Table S2). The inherent porosity appears to compensate for the roughness of the GDL surface, resulting in a relatively even surface and uniform layer thickness across the sliced region (width 3 µm). In contrast, Cu-

CF films (Figure 2d-f) demonstrate uniform thickness at lower loadings, but at higher loadings, they adopt a 'lobed' structure in which features of the GDE surface are magnified.

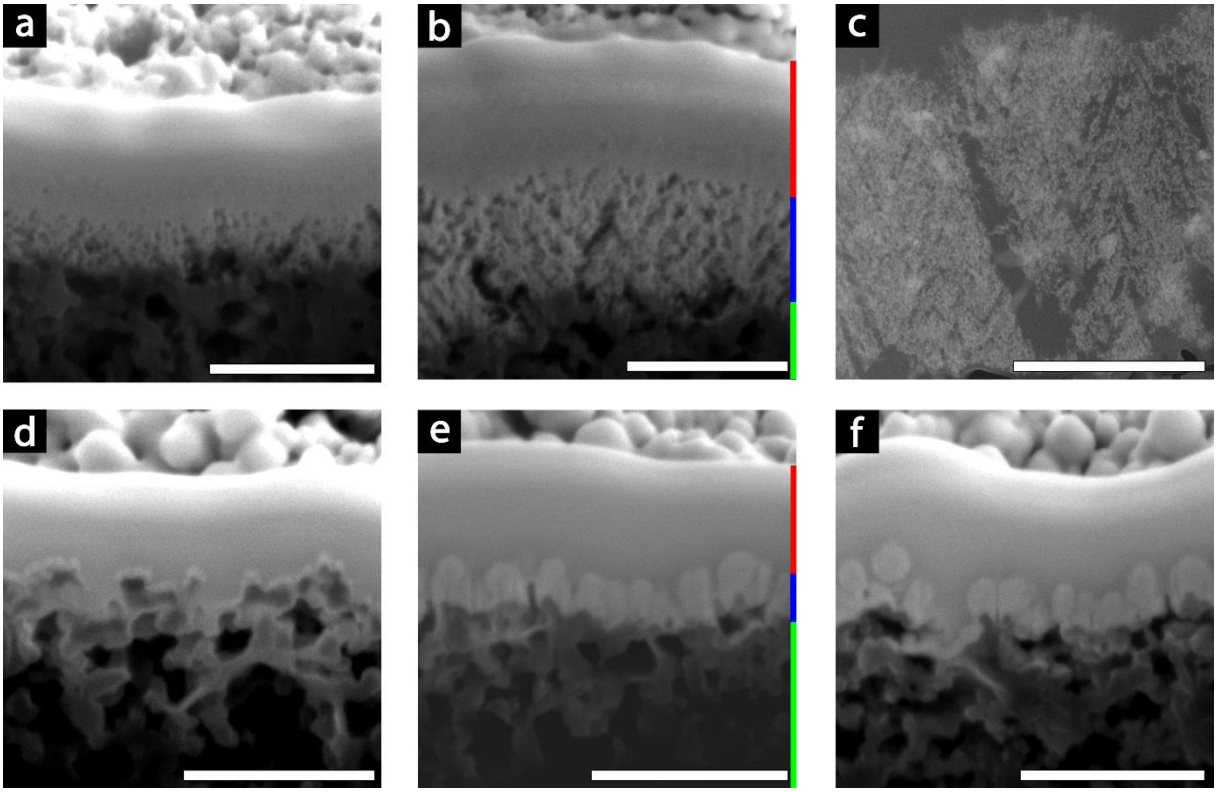

Figure 2 *FIB cross-sections of (a) Cu-NP-61, (b) Cu-NP-175, (d) Cu-CF-56, (e) Cu-CF-113 and (f) Cu-CF-203 with labeled layers in (b) and (e): Sigracet 39BB GDL (green), Cu-NP or Cu-CF layer (blue) and Pt protective layer (red). (c) TEM image of a FIB-lamella created from a vacuum impregnated Cu-NP-282 layer. The scale bar corresponds to 1 µm in all images.*

The geometrical relationship between CL thickness (L_{CL}) and the total mass loading (m_{NCs}) can be used to obtain the CL's porosity ϵ:

$$\epsilon = 1 - \frac{m_{NCs}}{\rho_{Cu_2O} \times L_{CL}}$$

Given that both oxidation states are present in the Cu_xO-NP samples, the average density (6.00 -6.31 $g \cdot cm^{-3}$)[25] and molar mass values (143.091 – 79.545 $g \cdot mol^{-1}$)[26] for a Cu_2O/CuO (0.76:0.24) mixture (see Table S1) were used to calculate m_{NCs}. Solving the equation above for ϵ, the porosity of Cu_xO-NP-64, -175 and -282 was determined to be 65.5, 65.0 and 65.9% respectively, which is higher than the typically assumed 0.4-0.5 range for porosities in fuel-cell and CO electrolyzer CL modeling studies,[27] but in the same range of reports on drop-cast Ag NP-based catalyst layers (68%) and carbon-fiber structures (70.6%).[12,28,29]

In order to visualize the CL porous architecture and corroborate the porosity values obtained from the cross-sections, we employed electron tomography, a technique whereby scanning transmission electron microscopy (STEM) images taken at different tilt angles are combined to create a three-dimensional (3D) representation of the original sample (Figure S7).[30,31] To that end, a sample of Cu_xO-NP-282 was vacuum impregnated using epoxy resin. Subsequently, a FIB-needle was cut out along the direction of the GDL surface in the bulk of the CL (Figure S8). Tilt series (one covering the full 180°) were then acquired from two distinct regions of interest in the needle, as annotated in Figure 3a (Supporting Note 3). Finally, magnified high resolution scanning transmission electron microscopy (HR-STEM) imaging revealed Cu_2O nanocrystals (Figure 3c and Figure S9).

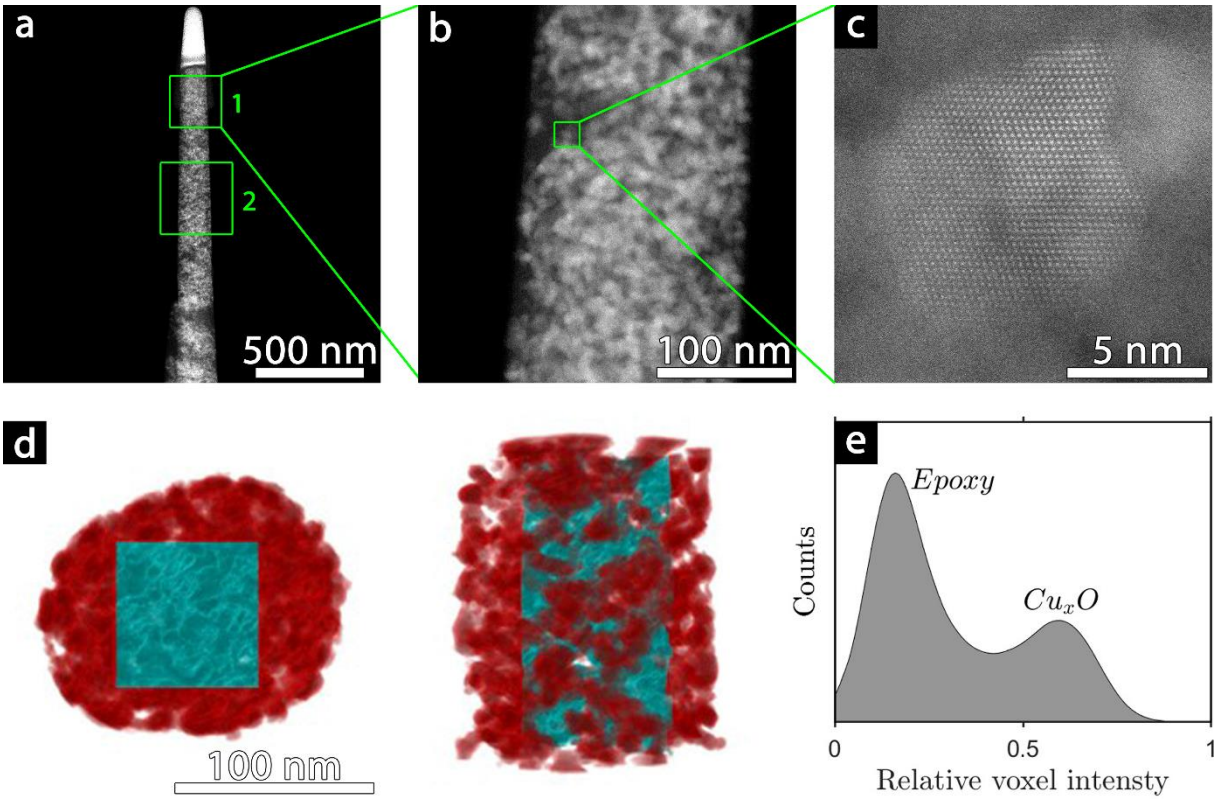

Figure 3 *(a) STEM image of the FIB needle with indicated regions of interest of the tomography series; (b) STEM image of a magnified region of the FIB lamella; (c)HR-STEM image taken from the Cu-NP-282 sample. The corresponding FT is depicted in* ***Figure S9****; (d) top and side view of a 3D reconstruction of the FIB-needle, with the beam-shaped volume from which the relevant parameters are determined indicated in blue; (e) histogram showing the relative voxel intensities taken from the beam shaped volume (indicated in blue) in the 3D reconstruction shown in* ***Figure 3d****, with indication of the epoxy/void and Cu_xO regions.*

In the interest of resolving the solid and void fractions, the 3D volumes resulting from reconstruction (e.g. in Figure 3d) were segmented. To avoid the influence of potential artifacts induced by the FIB, a beam-shaped volume (Figure 3d) entirely comprised within the needle was defined and used as base for segmentation and subsequent quantification. The value of each

voxel was normalized to a value between 0 and 1, after which all voxels were binned based on their normalized voxel intensity. In the resulting histogram (Figure 3e) two distinct regions can be defined, namely 'epoxy' and 'Cu_xO' voxels. The relative intensity value at the local minimum between these two regions is selected as the threshold for segmentation, whereby each voxel is classified as either Cu_xO lattice (solid) or epoxy (void). Videos of the resulting tomography reconstructions can be found in Supporting Movies SM01 and SM02.

That analysis yielded a mean porosity ϵ of 66.1 ± 0.3%. In addition, the 3D reconstruction of the surface enabled us to quantify the specific surface area a of Cu_xO-NP at 94 ± 10 $m^2 \cdot g^{-1}$ [$(1.94 \pm 0.20) \cdot 10^8$ $m^2 \cdot m^{-3}$]. By assuming the CL volume (of porosity ϵ) is comprised of randomly packed spherical particles with a specific surface area a, the effective packing diameter d_p

$$d_p = \frac{6(1-\epsilon)}{a}$$

was estimated at 10.6 ± 1.2 nm. For comparative purposes, we attempted to quantify the Brunauer-Emmett-Teller (BET) surface area from argon physisorption measurements directly on Cu-CF-201 and Cu_xO-NP-175 but the analysis did not yield conclusive results (Supporting Note 4, Figure S10). Instead, it exposed issues related to the limited sample size and to the heterogeneous and complex porous nature of the nanoscopic carbon/Cu interface involved.

Clearly, having an accurate estimate of the internal specific surface area – which dictates the real current density, cathode overpotential and thus reaction selectivity - is of great importance for electrocatalytic studies. Having established that the porosity was roughly constant regardless of CL thickness, this implied that the ratio of internal to external surface area – i.e. roughness - scaled linearly with loading. To determine whether this held true under operating conditions, an *in-situ* XAS study was carried out to probe the structural stability and oxidation state of Cu_xO-NP under bias. Figure 4a gives a schematic of the spectroelectrochemical cell configuration and the position of the CL with respect to the incident X-ray beam.[32] After mounting the cell and electrodes into the beamline station in a dry state (under air), electrolyte was pumped into the cell to obtain the oxidation state at open-circuit potential (OCP). Then, the Si_3N_4/Ti/Au/Cu_xO-NP working electrode was biased to a fixed negative potential (-0.1 V vs. RHE) to reduce the oxide. The potential was then held for 6 minutes to carry out the absorption experiment. Then, the potential was ramped up by 100 or 200 mV, followed by a scan at 50

$mV \cdot s^{-1}$ between the new potential set-point and the lowest potential vertex (-0.1 V vs. RHE) to establish a cyclic voltammogram, with the final one (-0.1-0.88 V vs. RHE) shown in Figure 4b. Figure 4c demonstrates that the nanoporous CL maintained its *ex-situ* oxidation state after initial exposure to OCP under alkaline conditions (0.1 M NaOH, pH ~13). Upon biasing to -0.08 V vs. RHE, the probed volume fully reduced to Cu(0) without any appreciable intensity loss or gain. This suggests that neither dissolution nor compaction of the CL (due to the higher density of Cu relative to Cu_2O) took place in the probed region. As the electrode potential was scanned in positive direction beyond 0.5 V vs. RHE, the CL oxidized and returned to its initial Cu(I) state at OCP. From this we have concluded that there were no or limited structural modifications in the probed region of the CL (indicated in Figure 4a) after exposure to electrolyte/biasing.

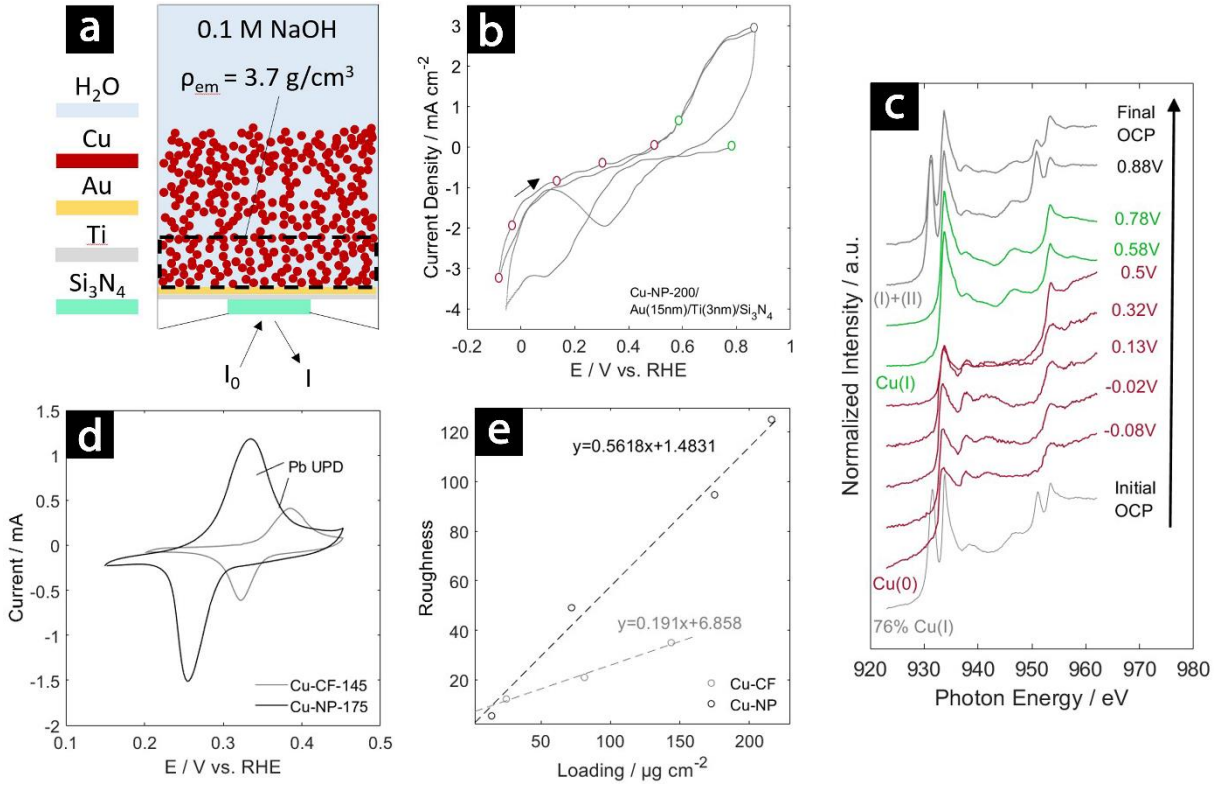

Figure 4 In-situ spectroelectrochemical analysis *(a) schematic of the electrochemical cell configuration, the X-ray beam is normal (angles exaggerated for sake of figure) to the 100 nm-thick Si_3N_4 window. A thin Ti (3 nm) and Au (15 nm) serve as current collectors. Cu loading = 200 $\mu g \cdot cm^{-2}$. Taking into account the effective porous medium density of the probed volume (ρ_{em} = 3.7 $g \cdot cm^{-3}$) and properties of water (0.1 M NaOH), the calculated X-ray attenuation depth is 180 nm. (b) cyclic voltammogram (50 $mV \cdot s^{-1}$) extracted after the final applied potential step. (c) Cu $L_{3,2}$-region as a function of applied potential (corrected for pH and ohmic resistance). (d) representative Pb underpotential deposition traces for Cu-CF-145 and Cu-NP-175. (e) ratio of real to geometric surface area (roughness) as a function of loading for Cu-CF and Cu-NP.*

To quantify the electrochemically available surface area of the CL under reduced conditions, Pb-UPD measurements were also carried out. The analysis revealed a clear correlation between electrode loading and the charge associated with monolayer coverage by Pb for Cu-CF and Cu_xO-NP (Figure S11). For example, the calculated areas for Cu-CF-145 and Cu_xO-NP-175,

whose CV traces are shown in Figure 4d, were 27.5 and 74.3 cm^2. The Cu-CF UPD peak potential and its larger degree of reversibility are indicative of a more uniform (111) texture, whereas the marked negative shift in peak potential and larger peak irreversibility of Cu_xO-NP are ascribed to its polycrystalline, irregular and nanoporous nature.[33] The calculated roughness factors (with respect to the exposed geometric surface area of 0.785 cm^2 during Pb-UPD) were 35.0 and 94.6, respectively (Table S4). For Cu_xO-NP-175, the Pb-UPD derived specific surface area was therefore 42.5 $m^2 \cdot g^{-1}$, which corresponds to 45.2% of the *ex-situ* value measured by electron tomography. That partial utilization may be ascribed to incomplete saturation of the entire porous structure with electrolyte, or to morphological changes in the upper layers of the CL, which were not probed by *in-situ* XAS.

We then proceeded to investigate how roughness affected COR under a limited set of experimental conditions. The performance of Cu_xO-NP was compared again with the nonporous yet rough Cu-CF benchmarks. A one-sided zero-gap electrolyzer configuration (Figure S12) was employed in all measurements. Importantly, active differential pressure control was used to equalize the pressures between the anolyte gas headspace and the cathode gas-liquid divider. That improved both membrane and the ionomer-free CL wetting and lowered both the total ohmic resistance and cell voltage (Figure S13).

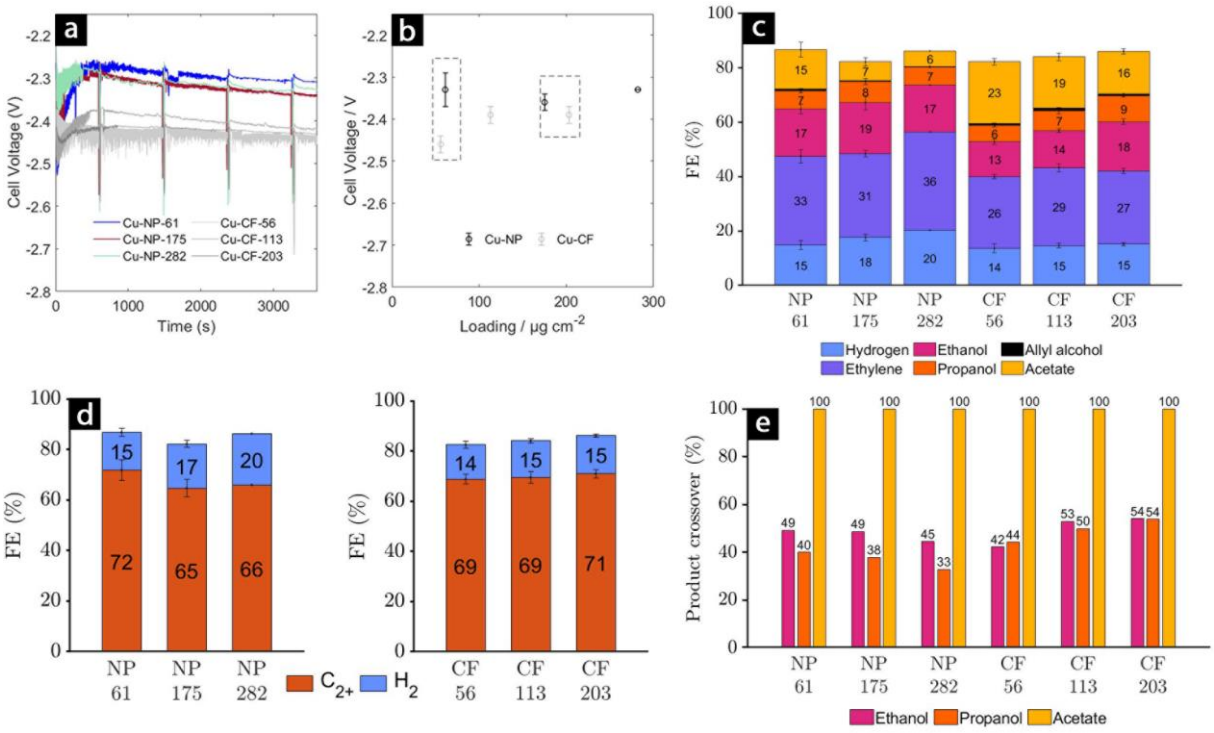

Figure 5 *(a) cell voltages as a function of time during 1 hour of chronopotentiometry at 50 mA·cm^{-2}, the voltage spikes correspond with gas injections to the in-line GC (b) corresponding cell voltage (for tabulated values see* ***Table S5****) and (c)*

*faradaic efficiency (for tabulated values see **Table S6**). (d) C_{2+} and H_2 faradaic efficiency. See also **Supporting Note 5**, **Figure S14**. (e) Share of alcohol and acetate product crossover for Cu-NP and Cu-CF CLs.*

Figure 5a depicts the voltage response recorded during galvanostatic CO reduction at -50 $mA \cdot cm^{-2}$ over Cu_xO-NP and Cu-CF. It is shown that Cu_xO-NP CLs yielded lower cell voltages overall, with an average reduction of 130 mV between Cu_xO-NP-61 and Cu-CF-56 (Figure 5b). As the same geometric current densities have been applied, the lower cell voltage is explained by the 2-fold higher roughness of Cu_xO-NP-61 (as calculated from the correlation in Figure 4e). While the average cell voltages are always lower for Cu_xO-NP, the deviation decreases to just 30-60 mV on average at higher loadings/roughness, which is an indication that other effects such as electrolyte uptake and mass transport become more important.

Figure 5c shows the corresponding Faradaic Efficiencies (FEs) after 1 hour of chronopotentiometry. Contrary to the Cu-CF CLs, which display no discernible trend across different loadings in terms of FE towards the competing Hydrogen Evolution Reaction (HER), the Cu_xO-NP CLs show a clear increase in hydrogen FE from 15% to 20% between the lowest (61 $\mu g \cdot cm^{-2}$) and highest (282 $\mu g \cdot cm^{-2}$) loading. When we inspected the visual appearance of Cu-CF after reaction, the formation of a blue precipitate, most likely $Cu(OH)_2$, was observed (Figure S15a). XAS analysis revealed that Cu-CF was fully oxidized to Cu(II) (Figure S16). In contrast, Cu_xO-NP-175 still consisted of about 28% Cu(I) (Table S1). As we actively lowered the CL pH by co-feeding CO_2 - which reacts with hydroxyl ions and forms bicarbonate that acts as a buffer - the Cu(I) contribution was found to increase (Figure S17) and the color changed to green (Figure S15b). Cu-CF CLs were less responsive to that change and remained fully oxidized. From those indirect observations we inferred that the CL pH was higher for Cu-CF, which explains the lower hydrogen FE.[34,35] Additional analysis of individual inline GC samples taken every 15 minutes indicated a clear rise in hydrogen production over the course of the measurements for Cu_xO-NP CLs, while no such trend was observed for Cu-CF. At the same time, contact angle measurements (Figure S18) showed a pronounced decrease in apparent contact angle for used Cu_xO-NP-175. We hypothesize that crack formation in the thicker nanoporous films (as seen for Cu_xO-NP-282 in Figure 2e) likely leads to increased hydrophilicity and imbibition of the Cu_xO-NP CLs over time,[36] which impedes CO mass transport and gradually promotes the HER.

The downward trend in acetate production with increasing Cu loading within the Cu_xO-NP and Cu-CF series is also clear. In general, Cu_xO-NP CLs exhibit lower acetate FEs compared to Cu-CF, indicating a possible influence due to surface texture. However, although the stronger

Cu(111) UPD signature of Cu-CF does point out towards stronger adsorption of OH*, which is a key intermediate in the acetate pathway,[37] acetate FEs (15% for Cu_xO-NP-61 and 16% for Cu-CF-203) were comparable owing to the similar magnitude of film thicknesses (about 370 nm). In contrast, Cu_xO-NP-61 and Cu-CF-56 had nearly identical Cu loadings but the CL thickness and roughness of the former was 10- and 2-fold higher, respectively, leading to a drop in selectivity of 8%.That loss of acetate FE is compensated by an increase in ethylene, ethanol and propanol FE (Figure 5d), so that Cu-CF films maintain the total C_{2+} FE also at higher loadings (68 ± 1.9% versus 70.9 ± 1.8% for loadings of 56 and 203 $\mu g \cdot cm^{-2}$, respectively). Cu_xO-NP CLs show a similar trend, but the HER contributes an additional 2-5% FE there. Using the quantitative values derived from the *in-situ* analysis we find that the ratio of ethylene, ethanol and propanol FE-to-acetate FE increases with roughness. However, whereas the relative error of that ratio falls below 7.1% for Cu-CF, it reaches 25.5% on average for Cu_xO-NP (Figure S19).

Due to the expected crossover of acetate through the anion exchange membrane,[38,39] a minimal volume of anolyte was used and recirculated during the measurements to facilitate liquid chromatography analysis. Indeed, while acetate crossover was ostensibly always at 100%, the extent of alcohol crossover (allyl alcohol is omitted in this analysis because of its low FE ≤ 1%) varied between 33% and 54% (Figure 5e). Thicker Cu_xO-NP films exhibited less crossover of ethanol and propanol, which we ascribe to the greater diffusion length and larger area for liquid-gas mass transport (evaporation). In contrast, Cu-CF films showed the reverse trend, their non-porous nature resulting in a closer proximity of the phase boundaries to the membrane for thicker films.[40] We further report that propanol crossover was 14% lower for equal CL thickness (Cu_xO-NP-61 vs Cu-CF-203) and 21% lower for the thickest Cu_xO-NP CL. The enhanced evaporation suggests that at least some inner pore surfaces in Cu_xO-NP are partially saturated, *i.e.* covered by just a few-nanometers thin electrolyte layer, which could dramatically affect gas solubility and mass transport. Therefore, devising complementary operando protocols for measuring saturation and its effects on reaction kinetics and mass transport during electrosynthesis over nanoporous Cu-based CLs could form the scope of future work.

In conclusion, Cu_2O and CuO nanocrystals with sub-10-nm dimensions were fabricated through a gas aggregation process and then assembled by soft landing to form catalyst layers on carbon-based gas diffusion layers. A FIB needle was extracted from a vacuum impregnated electrode and analyzed using electron tomography, resulting in 3D representations of the catalyst layer with nanometer resolution. Following segmentation, the porosity and specific surface area of the catalyst layers were determined to be 66.1 ± 0.3% and 94 ± 10 $m^2 \cdot g^{-1}$, respectively. Cross-sectional SEM analysis coupled with ICP-MS measurements yielded identical porosity values. By combining the quantitative properties derived from the tomographic reconstruction and the *in-situ* electrochemical analysis, it was found that on average, thick nanoporous CLs effectively utilized 45.2-48.3% of their as-prepared surface area. Moreover, a correlation between Cu loading and roughness was established that rationalized trends in product formation and transport during CO reduction. Our work has demonstrated how to visualize and quantify the porosity, surface area and utilization of a composite, nanoporous material interface, which is otherwise difficult to resolve using conventional techniques. The analysis is therefore applicable to a wide variety of nanoporous noble- and transition metal (oxide) layers in optoelectronic and catalytic applications.

ASSOCIATED CONTENT

Supporting Information. Experimental methods, AFM image, (in-situ) XPS and XAS spectra including analysis, cyclic voltammograms, graphic on ET, TEM image, FFT, ET acquisition details, Ar sorption including analysis, Pb UPD measurements, electrochemical reactor design, results from eCOR, images of degraded GDEs and contact angle measurements (.pdf); movies of the tomographic reconstructions (.mpg).

ACKNOWLEDGEMENT

The authors acknowledge financial support from NFFA-NEP - European Union's Horizon 2020 research and innovation program under grant agreement No. 101007417, proposal ID 159, and by the European Research Council (ERC CoG No. 815128 RealNANO) to Sara Bals. G.T.-C. acknowledges funding from the Comunidad Autónoma de Madrid (grant No. PEJ-2021-AI/IND-21143). This work has been partially funded by grant No. PID2023-149077OB-C31 funded by MCIN/AEI/10.13039/501100011033 and grant No. PLEC2021-007906 funded by MCIN/AEI/10.13039/501100011033 by the "European Union NextGenerationEU/PRTR". Partial funding by Photosurf-CM (Y2020/NMT-6469) project funded by Comunidad Autónoma de Madrid and cofinanced by European Structural Funds is also acknowledged.

REFERENCES

(1) Hu, Q.; Yang, K.; Peng, O.; Li, M.; Ma, L.; Huang, S.; Du, Y.; Xu, Z.-X.; Wang, Q.; Chen, Z.; Yang, M.; Loh, K. P. Ammonia Electrosynthesis from Nitrate Using a Ruthenium–Copper Cocatalyst System: A Full Concentration Range Study. *J. Am. Chem. Soc.* **2024**, *146* (1), 668–676. https://doi.org/10.1021/jacs.3c10516.

(2) de Luna, G. S.; Sacco, A.; Hernandez, S.; Ospitali, F.; Albonetti, S.; Fornasari, G.; Benito, P. Insights into the Electrochemical Reduction of 5-Hydroxymethylfurfural at High Current Densities. *ChemSusChem* **2022**, *15* (13), e202102504. https://doi.org/10.1002/cssc.202102504.

(3) Naseem, F.; Lu, P.; Zeng, J.; Lu, Z.; Ng, Y. H.; Zhao, H.; Du, Y.; Yin, Z. Solid Nanoporosity Governs Catalytic CO2 and N2 Reduction. *ACS Nano* **2020**, *14* (7), 7734–7759. https://doi.org/10.1021/acsnano.0c02731.

(4) Wang, L.; Nitopi, S.; Wong, A. B.; Snider, J. L.; Nielander, A. C.; Morales-Guio, C. G.; Orazov, M.; Higgins, D. C.; Hahn, C.; Jaramillo, T. F. Electrochemically Converting Carbon Monoxide to Liquid Fuels by Directing Selectivity with Electrode Surface Area. *Nat Catal* **2019**, *2* (8), 702–708. https://doi.org/10.1038/s41929-019-0301-z.

(5) Hursán, D.; Samu, A. A.; Janovák, L.; Artyushkova, K.; Asset, T.; Atanassov, P.; Janáky, C. Morphological Attributes Govern Carbon Dioxide Reduction on N-Doped Carbon Electrodes. *Joule* **2019**, *3* (7), 1719–1733. https://doi.org/10.1016/j.joule.2019.05.007.

(6) Zenyuk, I. V.; Das, P. K.; Weber, A. Z. Understanding Impacts of Catalyst-Layer Thickness on Fuel-Cell Performance via Mathematical Modeling. *J. Electrochem. Soc.* **2016**, *163* (7), F691. https://doi.org/10.1149/2.1161607jes.

(7) Steinbach, A. J.; Allen, J. S.; Borup, R. L.; Hussey, D. S.; Jacobson, D. L.; Komlev, A.; Kwong, A.; MacDonald, J.; Mukundan, R.; Pejsa, M. J.; Roos, M.; Santamaria, A. D.; Sieracki, J. M.; Spernjak, D.; Zenyuk, I. V.; Weber, A. Z. Anode-Design Strategies for

Improved Performance of Polymer-Electrolyte Fuel Cells with Ultra-Thin Electrodes. *Joule* **2018**, *2* (7), 1297–1312. https://doi.org/10.1016/j.joule.2018.03.022.

(8) Dinh, C.-T.; Burdyny, T.; Kibria, M. G.; Seifitokaldani, A.; Gabardo, C. M.; García de Arquer, F. P.; Kiani, A.; Edwards, J. P.; De Luna, P.; Bushuyev, O. S.; Zou, C.; Quintero-Bermudez, R.; Pang, Y.; Sinton, D.; Sargent, E. H. CO2 Electroreduction to Ethylene via Hydroxide-Mediated Copper Catalysis at an Abrupt Interface. *Science* **2018**, *360* (6390), 783–787. https://doi.org/10.1126/science.aas9100.

(9) Daems, N.; Choukroun, D.; Merino, P.; Rettenmaier, C.; Pacquets, L.; Bergmann, A.; Santoro, G.; Vázquez, L.; Martínez, L.; Roldan Cuenya, B.; Martín Gago, J. A.; Breugelmans, T. Steering Hydrocarbon Selectivity in CO_2 Electroreduction over Soft-Landed CuO_x Nanoparticle-Functionalized Gas Diffusion Electrodes. *ACS Appl. Mater. Interfaces* **2022**, *14* (2), 2691–2702. https://doi.org/10.1021/acsami.1c17998.

(10) Ortel, E.; Hertwig, A.; Berger, D.; Esposito, P.; Rossi, A. M.; Kraehnert, R.; Hodoroaba, V.-D. New Approach on Quantification of Porosity of Thin Films via Electron-Excited X-Ray Spectra. *Anal. Chem.* **2016**, *88* (14), 7083–7090. https://doi.org/10.1021/acs.analchem.6b00847.

(11) Wu, J.; Melo, L. G. A.; Zhu, X.; West, M. M.; Berejnov, V.; Susac, D.; Stumper, J.; Hitchcock, A. P. 4D Imaging of Polymer Electrolyte Membrane Fuel Cell Catalyst Layers by Soft X-Ray Spectro-Tomography. *Journal of Power Sources* **2018**, *381*, 72–83. https://doi.org/10.1016/j.jpowsour.2018.01.074.

(12) McLaughlin, D.; Bierling, M.; Moroni, R.; Vogl, C.; Schmid, G.; Thiele, S. Tomographic Reconstruction and Analysis of a Silver CO_2 Reduction Cathode. *Advanced Energy Materials* **2020**, *10* (19), 2000488. https://doi.org/10.1002/aenm.202000488.

(13) Shpigel, N.; Sigalov, S.; Malchik, F.; Levi, M. D.; Girshevitz, O.; Khalfin, R. L.; Aurbach, D. Quantification of Porosity in Extensively Nanoporous Thin Films in Contact

with Gases and Liquids. *Nat Commun* **2019**, *10* (1), 4394. https://doi.org/10.1038/s41467-019-12277-4.

(14) Van Ginkel, H. J.; Vollebregt, S.; Schmidt-Ott, A.; Zhang, G. Q. Mass and Density Determination of Porous Nanoparticle Films Using a Quartz Crystal Microbalance. *Nanotechnology* **2022**, *33* (48), 485704. https://doi.org/10.1088/1361-6528/ac7811.

(15) Rabinowitz, J. A.; Ripatti, D. S.; Mariano, R. G.; Kanan, M. W. Improving the Energy Efficiency of CO Electrolysis by Controlling Cu Domain Size in Gas Diffusion Electrodes. *ACS Energy Lett.* **2022**, *7* (11), 4098–4105. https://doi.org/10.1021/acsenergylett.2c01978.

(16) Kormányos, A.; Endrődi, B.; Zhang, Z.; Samu, A.; Mérai, L.; Samu, G. F.; Janovák, L.; Janáky, C. Local Hydrophobicity Allows High-Performance Electrochemical Carbon Monoxide Reduction to C2+ Products. *EES. Catal.* **2023**, *1* (3), 263–273. https://doi.org/10.1039/D3EY00006K.

(17) O'Brien, C. P.; McLaughlin, D.; Böhm, T.; Xiao, Y. C.; Edwards, J. P.; Gabardo, C. M.; Bierling, M.; Wicks, J.; Sedighian Rasouli, A.; Abed, J.; Young, D.; Dinh, C.-T.; Sargent, E. H.; Thiele, S.; Sinton, D. Scalability and Stability in CO2 Reduction via Tomography-Guided System Design. *Joule* **2024**. https://doi.org/10.1016/j.joule.2024.07.004.

(18) Johnson, G. E.; Colby, R.; Laskin, J. Soft Landing of Bare Nanoparticles with Controlled Size, Composition, and Morphology. *Nanoscale* **2015**, *7* (8), 3491–3503. https://doi.org/10.1039/C4NR06758D.

(19) Martínez, L.; Lauwaet, K.; Santoro, G.; Sobrado, J. M.; Peláez, R. J.; Herrero, V. J.; Tanarro, I.; Ellis, G. J.; Cernicharo, J.; Joblin, C.; Huttel, Y.; Martín-Gago, J. A. Precisely Controlled Fabrication, Manipulation and in-Situ Analysis of Cu Based Nanoparticles. *Sci Rep* **2018**, *8* (1), 7250. https://doi.org/10.1038/s41598-018-25472-y.

(20) Fernández-García, E.; Merino, P.; González-Rodríguez, N.; Martínez, L.; Pozo, M. del; Prieto, J.; Blanco, E.; Santoro, G.; Quintana, C.; Petit-Domínguez, M. D.; Casero, E.;

Vázquez, L.; Martínez, J. I.; Martín-Gago, J. A. Enhanced Electrocatalysis on Copper Nanostructures: Role of the Oxidation State in Sulfite Oxidation. *ACS Catal.* **2024**, *14* (15), 11522–11531. https://doi.org/10.1021/acscatal.3c05897.

(21) Spadaro, M. C.; Humphrey, J. J. L.; Cai, R.; Martínez, L.; Haigh, S. J.; Huttel, Y.; Spencer, S. J.; Wain, A. J.; Palmer, R. Electrocatalytic Behavior of PtCu Clusters Produced by Nanoparticle Beam Deposition. *J. Phys. Chem. C* **2020**, *124* (43), 23683–23689. https://doi.org/10.1021/acs.jpcc.0c06744.

(22) Ruano, M.; Martínez, L.; Huttel, Y. Investigation of the Working Parameters of a Single Magnetron of a Multiple Ion Cluster Source: Determination of the Relative Influence of the Parameters on the Size and Density of Nanoparticles. *Dataset Papers in Science* **2013**, *2013*, 1–8. https://doi.org/10.1155/2013/597023.

(23) Söderlund, J.; Kiss, L. B.; Niklasson, G. A.; Granqvist, C. G. Lognormal Size Distributions in Particle Growth Processes without Coagulation. *Phys. Rev. Lett.* **1998**, *80* (11), 2386–2388. https://doi.org/10.1103/PhysRevLett.80.2386.

(24) Grioni, M.; Goedkoop, J. B.; Schoorl, R.; de Groot, F. M. F.; Fuggle, J. C.; Schäfers, F.; Koch, E. E.; Rossi, G.; Esteva, J.-M.; Karnatak, R. C. Studies of Copper Valence States with Cu L_3 X-Ray-Absorption Spectroscopy. *Phys. Rev. B* **1989**, *39* (3), 1541–1545. https://doi.org/10.1103/PhysRevB.39.1541.

(25) Lide, D. R. *CRC Handbook of Chemistry and Physics, 90th Edition*; Taylor & Francis, 2009.

(26) Prohaska, T.; Irrgeher, J.; Benefield, J.; Böhlke, J. K.; Chesson, L. A.; Coplen, T. B.; Ding, T.; Dunn, P. J. H.; Gröning, M.; Holden, N. E.; Meijer, H. A. J.; Moossen, H.; Possolo, A.; Takahashi, Y.; Vogl, J.; Walczyk, T.; Wang, J.; Wieser, M. E.; Yoneda, S.; Zhu, X.-K.; Meija, J. Standard Atomic Weights of the Elements 2021 (IUPAC Technical

Report). *Pure and Applied Chemistry* **2022**, *94* (5), 573–600. https://doi.org/10.1515/pac-2019-0603.

(27) Disselkoen, K. R.; Rabinowitz, J. A.; Mani, A.; Kanan, M. W. Continuum Model for Optimizing CO Reduction Gas Diffusion Electrodes. *ACS Sustainable Chem. Eng.* **2024**, *12* (19), 7235–7245. https://doi.org/10.1021/acssuschemeng.3c05194.

(28) Jhong, H.-R. (Molly); Brushett, F. R.; Yin, L.; Stevenson, D. M.; Kenis, P. J. A. Combining Structural and Electrochemical Analysis of Electrodes Using Micro-Computed Tomography and a Microfluidic Fuel Cell. *J. Electrochem. Soc.* **2012**, *159* (3), B292–B298. https://doi.org/10.1149/2.033203jes.

(29) Weng, L.-C.; Bell, A. T.; Weber, A. Z. Modeling Gas-Diffusion Electrodes for CO_2 Reduction. *Phys. Chem. Chem. Phys.* **2018**, *20* (25), 16973–16984. https://doi.org/10.1039/C8CP01319E.

(30) Midgley, P. A.; Weyland, M. 3D Electron Microscopy in the Physical Sciences: The Development of Z-Contrast and EFTEM Tomography. *Ultramicroscopy* **2003**, *96* (3–4), 413–431. https://doi.org/10.1016/S0304-3991(03)00105-0.

(31) Weyland, M.; Midgley, P. A. Electron Tomography. *Materials Today* **2004**, *7* (12), 32–40. https://doi.org/10.1016/S1369-7021(04)00569-3.

(32) Nappini, S.; D'Amario, L.; Favaro, M.; Dal Zilio, S.; Salvador, F.; Betz-Güttner, E.; Fondacaro, A.; Píš, I.; Romanzin, L.; Gambitta, A.; Bondino, F.; Lazzarino, M.; Magnano, E. Soft X-Ray Spectroscopies in Liquids and at Solid-Liquid Interface at BACH Beamline at Elettra. *Rev Sci Instrum* **2021**, *92* (1), 015115. https://doi.org/10.1063/5.0025326.

(33) Hochfilzer, D.; Tiwari, A.; Clark, E. L.; Bjørnlund, A. S.; Maagaard, T.; Horch, S.; Seger, B.; Chorkendorff, I.; Kibsgaard, J. In Situ Analysis of the Facets of Cu-Based Electrocatalysts in Alkaline Media Using Pb Underpotential Deposition. *Langmuir* **2022**, *38* (4), 1514–1521. https://doi.org/10.1021/acs.langmuir.1c02830.

(34) Strmcnik, D.; Uchimura, M.; Wang, C.; Subbaraman, R.; Danilovic, N.; Van Der Vliet, D.; Paulikas, A. P.; Stamenkovic, V. R.; Markovic, N. M. Improving the Hydrogen Oxidation Reaction Rate by Promotion of Hydroxyl Adsorption. *Nature Chem* **2013**, *5* (4), 300–306. https://doi.org/10.1038/nchem.1574.

(35) Wuttig, A.; Yaguchi, M.; Motobayashi, K.; Osawa, M.; Surendranath, Y. Inhibited Proton Transfer Enhances Au-Catalyzed CO2-to-Fuels Selectivity. *Proceedings of the National Academy of Sciences* **2016**, *113* (32), E4585–E4593. https://doi.org/10.1073/pnas.1602984113.

(36) Kusoglu, A.; Kwong, A.; Clark, K. T.; Gunterman, H. P.; Weber, A. Z. Water Uptake of Fuel-Cell Catalyst Layers. *J. Electrochem. Soc.* **2012**, *159* (9), F530. https://doi.org/10.1149/2.031209jes.

(37) Li, C. W.; Ciston, J.; Kanan, M. W. Electroreduction of Carbon Monoxide to Liquid Fuel on Oxide-Derived Nanocrystalline Copper. *Nature* **2014**, *508* (7497), 504–507. https://doi.org/10.1038/nature13249.

(38) Gabardo, C. M.; O'Brien, C. P.; Edwards, J. P.; McCallum, C.; Xu, Y.; Dinh, C.-T.; Li, J.; Sargent, E. H.; Sinton, D. Continuous Carbon Dioxide Electroreduction to Concentrated Multi-Carbon Products Using a Membrane Electrode Assembly. *Joule* **2019**, *3* (11), 2777–2791. https://doi.org/10.1016/j.joule.2019.07.021.

(39) Zhang, J.; Luo, W.; Züttel, A. Crossover of Liquid Products from Electrochemical CO2 Reduction through Gas Diffusion Electrode and Anion Exchange Membrane. *Journal of Catalysis* **2020**, *385*, 140–145. https://doi.org/10.1016/j.jcat.2020.03.013.

(40) Monis Ayyub, M.; Kormányos, A.; Endrődi, B.; Janáky, C. Electrochemical Carbon Monoxide Reduction at High Current Density: Cell Configuration Matters. *Chemical Engineering Journal* **2024**, *490*, 151698. https://doi.org/10.1016/j.cej.2024.151698.